# An Interoperable and High-Efficiency Wireless Electric Vehicle Charger Based on Reconfigurable Topology

Baokun Zhang, *Student Member, IEEE*, Junjun Deng, *Member, IEEE*, and Zhenpo Wang, *Senior Member, IEEE*

***Abstract*—This work proposes a solution to enhance interoperability and maintain high efficiency throughout the entire charging process in inductive power transfer systems for wireless electric vehicle charging. A novel reconfigurable magnetic coupling resonant topology with a dual-coupled *LCC*-compensated structure is proposed. When facing diverse potential configurations on the secondary side, the adaptable topology provides flexibility in switching singular or dual coupled coils, as well as different compensation networks. This enhances both the magnetic and electrical interoperability of wireless chargers. Besides, an IPT system is proposed based on the reconfigurable topology on both primary and secondary sides. Utilizing two power transfer paths and four selector switches, the system can switch between three constant current (CC) modes and two constant voltage (CV) modes, ensuring load-independent characteristics. This feature facilitates the CC–CV and multistage constant current (MSCC) outputs. Moreover, multiple optimal load values are configured to ensure high efficiency across wide range of loads. Finally, experimental results demonstrate the measured dc–dc efficiency ranges from 91.1% to 94.6% with the MSCC profile as the dc load varies from 18.33 to 165 Ω. In contrast, the CC–CV charging profile yields efficiency ranging from 89.3% to 93.9%.**

***Index Terms*—Efficiency, inductive power transfer (IPT), interoperability, reconfigurable, wireless charger.**

## I. Introduction

INDUCTIVE power transfer (IPT) technique is a promising charging solution for the wireless charging of electric vehicles (EVs) due to its advantages of convenience and adaptability [1]. With the rapid advancement of the industrialization of wireless charging technology for EVs, the interoperability requirement is becoming increasingly important. Especially in public EV charging facilities, the transmitter (Tx) of wireless chargers mounted under the chassis should be compatible with multiple types of receivers (Rx) from various manufacturers with potentially different topologies [2].

Manuscript received 19 March 2024; revised 13 June 2024; accepted 4 July 2024. Date of publication 9 July 2024; date of current version 4 September 2024. This work was supported by the National Key Research and Development Program of China under Grant 2021YFB2501604. Recommended for publication by Associate Editor Y. Tang. *(Corresponding author: Junjun Deng.)*

The authors are with the National Engineering Research Center of Electric Vehicles, School of Mechanical Engineering, Beijing Institute of Technology, Beijing 100081, China (e-mail: bk.zhang@bit.edu.cn; dengjunjun@bit.edu.cn; wangzhenpo@bit.edu.cn).

Color versions of one or more figures in this article are available at https://doi.org/10.1109/TPEL.2024.3425603.

Digital Object Identifier 10.1109/TPEL.2024.3425603

Besides, the efficiency of EV chargers is concerning. IPT systems are supposed to maintain high efficiency throughout the charging process. It is challenging work because the equivalent load of batteries varies greatly in practical applications, while there is an optimum load with a fixed value for maximum efficiency [3]. As the actual equivalent load deviates from the optimum load, the efficiency decreases significantly. In the past decades, lots of effort has been made to comply with the above problems, and the major approaches are analyzed below.

### A. Literature Review

According to the standard SAE J2954, the interoperability requirements of IPT systems in terms of power are specified as follows: first, the ground assembly (GA) should be capable of transmitting power to vehicle assemblies (VAs); second, the delivered power should fulfill the demand. Subsequently, these two conditions are translated into the analysis of magnetic and electrical interoperability, respectively.

Magnetic interoperability is the basis for ensuring power transmission capability, and sufficient magnetic flux should be coupled between the transmission coils over the full range of coil positions. This involves the compatibility of different magnetic coupling coils. There are two basic types of coils, namely unipolar (such as rectangular and circular coil) and bipolar (such as DD coil), and they exhibit different patterns of magnetic flux. Unipolar coils generate the perpendicular magnetic flux, and the excitation generates only one pair of polarity; while bipolar coils generate the parallel magnetic flux, and the excitation generates two pairs of magnetic polarities [4]. Since the directions of magnetic flux are perpendicular, the unipolar and bipolar coils are decoupled at aligned positions and show poor interoperability [5]. Considering the magnetic coupling of the unipolar and bipolar coils is improved under the misaligned conditions, an adaptive position adjustment method is proposed to improve the interoperability of the two coils [6]. Still, the mutual inductance or coupling coefficients on the numerical grade may not always meet the power transfer requirements [7], especially when compared to coil combinations of the same type.

Some work has been devoted to developing new coils and topologies to achieve compatibility with the two basic coils. By introducing mutually decoupled coils to the existing coils, the multicoils are developed, such as double-D quadrature pad [8], bipolar pad [9], and triple quadrature pad [10] coil structures.

According to the phase and direction of the excitation current, different flux patterns are generated [11], including perpendicular flux pattern, parallel flux pattern, and perpendicular–parallel flux pattern. Therefore, magnetic interoperability with the basic coils is guaranteed. However, the above multicoils require two independent inverters to control the excitation current separately or simultaneously, which increases the cost and volume of the system. Recently, several new topologies have been developed to achieve interoperability with the basic coils. It is done by combining the novel coil structures with the corresponding power electronics [12], [13], for example, the quadrupole coil with series-connected diode rectifier [14], and two adjacently placed unipolar coils with a three-switch dual-output inverter [15]. While these methods demonstrate improved magnetic interoperability (and anti-misalignment performance), they entail notable additional costs, including decoupling windings, compensation components, dc-link capacitors, and power devices.

Electrical interoperability determines whether the target power can be transmitted, and it is described by an interface impedance-based approach [16]. The impedance of the VA ($Z_{\mathrm{VA}}$) is presented to the interface of the GA and forms $Z_{\mathrm{GA}}$. Only if the transformed $Z_{\mathrm{GA}}$ impedance lies within the GA electronic capability, the requested power can be delivered to the VA [17]. To adapt to different VAs and operating conditions, while keeping $Z_{\mathrm{GA}}$ within the allowable impedance range, two ways are proposed to improve electrical interoperability. One way is preparing the GA electronics with a wider driving range. However, such redundant configurations significantly increase the cost of the system. Another way aims to reduce the electrical burden on GA electronics by impedance adjusting, such as tunable matching networks (TMN) using tunable reactance elements [18]. Although the effectiveness of this solution is validated, two limitations are observed. First, it requires complicated real-time control for the adjustment of tunable elements to desired values. Second, the design of the TMN based on *LCC* networks primarily addresses wide operating conditions rather than diverse compensation networks from various Rx configurations.

In addition to power, efficiency is also an important indicator of wireless chargers. Considering that the equivalent load of the battery varies during charging, maintaining high efficiency over a wide load range is the so-called maximum efficiency point tracking (MEPT) [3], and the key is to realize load matching. Its principle is to map the actual load to the optimal resistance of the secondary circuits, so as to improve the operating efficiency of the resonant network. Since load matching cannot be achieved solely by the inverter on the primary side, the prevalent methods are utilizing power converters on the secondary side. For ease of discussion, $\lambda$ is denoted as the ratio of equivalent resistance of the ac ports of compensation networks to the dc load of batteries, and it is a function of control variables for power converters. Therefore, by controlling the power converter, not only the output parameters can be adjusted to follow the charging profile, but also the equivalent resistance is adjusted to the optimal load value to achieve load matching. The most common practice is to cascade a dc–dc converter at the back end of the rectifier [19], [20], and $\lambda$ varies with the duty cycle. However, the multistage power conversion inevitably brings in additional power loss as well as increased cost and size. Another choice is utilizing active rectifiers. Since $\lambda$ is the function of the duty cycle and phase angle of the secondary-side rectifier [21], load matching is realized by controlling the phase shift angles of the primary and secondary converters, and the efficiency of resonant networks is kept at a high level. Nevertheless, such dual-phase-shift control methods still suffer hard-switching and non-negligible switching losses under light load [22]. Recently, another practical method has been proposed with low cost and uncomplicated control. By selecting the operating mode of the active rectifier [23] or by replacing a diode of the rectifier with one MOSFET device [24], [25], the rectifier operates in full-bridge mode and half-bridge mode, with the ratio $\lambda$ changed from $8/\pi^2$ to $2/\pi^2$. Since there are only two available modes with fixed ratios, this method may have limitations in the face of large load variation.

Besides, the effect of charging modes on efficiency needs to be discussed. Li-ion batteries are widely used in EVs, and a typical charging profile for Li-ion batteries includes constant current (CC) charging followed by constant voltage (CV) charging [26], [27]. With the CC–CV charging profile, the equivalent resistance of the battery experiences continuous variations over a wide load range. As an alternative to the conventional CC–CV mode, the multistage constant current (MSCC) charging mode has advantages including longer cycle life, higher charge energy efficiency, and shorter charging time [28], [29]. Its charge profile is composed of several CC mode stages of which current amplitudes are different and the current at each stage is applied to the battery until the voltage of the battery reaches its cut-off value [30]. Several studies have investigated the implementation of the MSCC method in IPT systems [31], [32], [33]. By employing the MSCC charging profile, the battery's equivalent resistance is segmented into discrete intervals, resulting in a narrower operational range compared to that with the CC–CV profile. This reduction in the range of variation alleviates the difficulty of MEPT. Consequently, the MSCC charging mode holds promise for maintaining high efficiency throughout the charging process.

In summary, various techniques have been developed to address individual problems. However, to the best of the authors' knowledge, a method that simultaneously enhances magnetic interoperability, electrical interoperability, and charging efficiency is still lacking.

### B. Contributions

The purpose of this work is to achieve interoperability with diverse Rx configurations and ensure high efficiency throughout the charging process. This is accomplished by reconfiguring and matching of transmission coils, along with compensation components. The main contributions of this work are summarized as follows.

1) A novel dual-coupled resonant topology is proposed, where both the main inductor and compensation inductor can transmit power individually or jointly. The integrated coils are compatible with both unipolar and bipolar coils, ensuring magnetic interoperability.

2) By reconfiguring the compensation networks and transmission coils, the proposed topology adapts to diverse operating conditions and Rx configurations with various compensation networks. This adaptation reduces the required power capacity on inverters and enhances its electrical interoperability.
3) An IPT system based on the reconfigurable topology is designed. It is capable of implementing both CC–CV and MSCC charging profiles. By configuring optimal loads for each charging stage properly, MEPT is achieved during the whole charging process.

The rest of this article is organized as follows. Section II presents the analysis of the proposed interoperable reconfigurable topology. Section III discusses the equivalent load during the charging process. In Section IV, the reconfigurable topology-based IPT system is proposed. Section V outlines the design procedure of high-efficiency IPT systems with two typical charging profiles. Experimental verification of a prototype is presented in Section VI. Finally, the work is concluded in Section VII.

## II. Proposed Interoperable Reconfigurable Topology

As analyzed in the last section, if the same type of transmission coils can be matched, it will help to couple sufficient magnetic flux without the development of multicoils that can be compatible with two basic coils. Besides, considering that the presented impedance $Z_{\mathrm{GA}}$ is affected by the compensation networks, if the compensation circuits of Tx and Rx are compatible with each other, the electrical burden on the GA electronics can be eased or even eliminated, thus improving electrical interoperability. Therefore, it is important to realize the combination and matching of transmission coils and compensation components, and the design principles are listed as follows.

1) Do not introduce additional passive components, and the number of selector switches should be minimized.
2) The topology should be stocked with basic coils (unipolar and bipolar) to match different Rx coils.
3) The topology should be adapted to the mainstream compensation networks for EV charging applications, such as S and P topology (basic compensation), and *LCL* and *LCC* topology (high-order compensation).

With the above design concept in mind, the proposed novel reconfigurable magnetic coupling resonant topology is shown in Fig. 1(a). $L_1$ and $L_{\mathrm{f1}}$ represent the main inductor and compensation inductor, respectively, and they are integrated to reduce the size of wireless chargers, $C_1$ and $C_{\mathrm{f1}}$ are compensation capacitors, and $K_1$ and $K_2$ are selector switches, where $K_2$ is a single-pole double-throw (SPDT) switch. The topology is connected to a high-frequency inverter through two ac ports. And the topology parameters are designed by the following equations to achieve a constant resonant angular frequency $\omega$:

$$L_{\mathrm{f1}}C_{\mathrm{f1}} = 1/\omega^2 \tag{1}$$

$$(L_1 - L_{\mathrm{f1}})\,C_1 = 1/\omega^2. \tag{2}$$

Compared with the conventional *LCC*-compensated topology, the proposed topology features a magnetically coupled compensation inductor, allowing it to serve both as a compensation element and another power transmission path. Besides, the proposed topology does not introduce other components except the selector switches. Nowadays, advanced products such as solid-state relays [34] or bidirectional power switches [35] have external dimensions of only a few centimeters, even for high-current applications, and can be easily integrated into inverters. Consequently, the proposed topology does not lead to a bulky size.

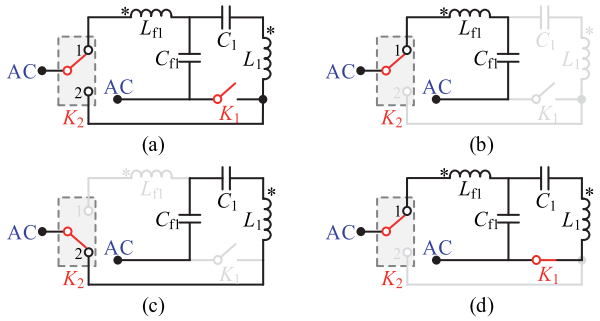


Fig. 1. (a) Proposed reconfigurable topology and (b)–(d) three operating modes.

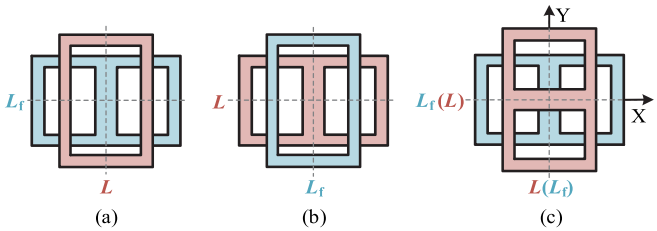


Fig. 2. Integrated coil schemes, in which the same-side cross-coupling effect can be neglected. (a) Main inductor is unipolar and the compensation inductor is bipolar. (b) Main inductor is bipolar and the compensation inductor is unipolar. (c) Both the main inductor and compensation inductor are bipolar.

Thanks to two available power transfer paths as well as two selector switches, the proposed topology operates in three modes, corresponding to different transmission coils and compensation components. Fig. 1(b)–(d) shows the ON–OFF state of the switches in each mode, as well as the inductors and capacitors connected to the inverter.

1) When $K_{21}$ is closed, the compensation network operates as a conventional S topology.
2) When $K_{22}$ is closed, the compensation network operates as another S topology.
3) When $K_1$ and $K_{21}$ are closed, the compensation network operates as a dual-coupled *LCC* topology.

Considering the same-side cross-coupling does not contribute to power transfer, the coupling coefficient $k_{1\mathrm{f1}}$ between $L_1$ and $L_{\mathrm{f1}}$ should be minimized or eliminated. Aiming at this issue, the coil integrated methods are referred to in papers [36], [37], [38] and presented in Fig. 2. In particular, the scheme (a) and (b) meet the requirements of the second design principle.

As shown in Fig. 3(a), the important impedance interfaces for interoperability assessment include $Z_{\mathrm{in}}$ and $Z_{\mathrm{GA}}$. The drive capability of the inverter is described by the inverter capability

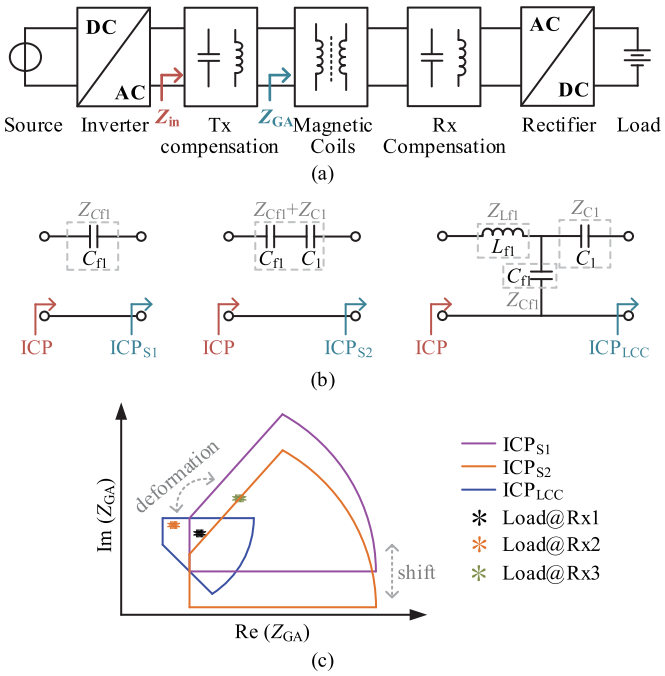


Fig. 3. (a) Key impedance interfaces of IPT systems. (b) Three available primary compensations by topology reconfiguration. (c) Schematic diagram of ICP and different operating points on the impedance plane of $Z_{GA}$ [17].

plane (ICP). Then ICP is transferred from the $Z_{in}$ interface to the $Z_{GA}$ interface. At the same time, different loads of the Rx are transferred to the $Z_{GA}$ interface. Finally, in the impedance plane of the $Z_{GA}$ interface, only the operating points within the ICP can be driven by the inverter.

In practical applications, the potential topologies of Rx may be various, so high compatibility of the Tx is required. Luckily, by turning ON or turning OFF the selector switches, the proposed topology can be converted to different types, as shown in Fig. 3(b). The impedance for ICP transferred from the $Z_{in}$ interface to the $Z_{GA}$ interface is derived as follows:

$$Z_{GA\_S1} = Z_{in} - Z_{Cf1} \tag{3}$$

$$Z_{GA\_S2} = Z_{in} - Z_{Cf1} - Z_{C1} \tag{4}$$

$$Z_{GA\_LCC} = Z_{Cf1} \cdot Z_{Lf1}/Z_{in} - Z_{Cf1} - Z_{C1}. \tag{5}$$

The primary compensation causes a shift or deformation of the ICP on the impedance plane in the complex plane. For the Tx equipped with the same inverter and different compensation networks, the corresponding ICP as well as the operating points that can be driven is also different [17], as shown in Fig. 3(c). Therefore, by the reconstruction of the compensation topology, the proposed method is compatible with a wider region of the impedance plane, both in real and imaginary parts. In contrast, using TMN on the primary side can also realize the deformation of the ICP by adjusting $Z_{Lf1}$, but it requires more complicated real-time control.

Furthermore, taking the integrated coil scheme (b) in Fig. 2 as an example, Fig. 4 shows three available configurations in turn: S-compensation with the unipolar coil, S-compensation

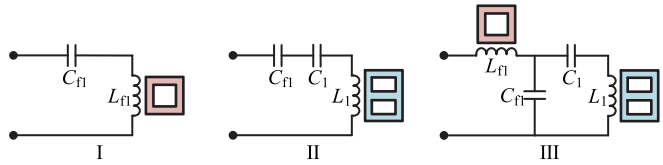


Fig. 4. Available configurations of Tx using the integrated coil scheme (b).

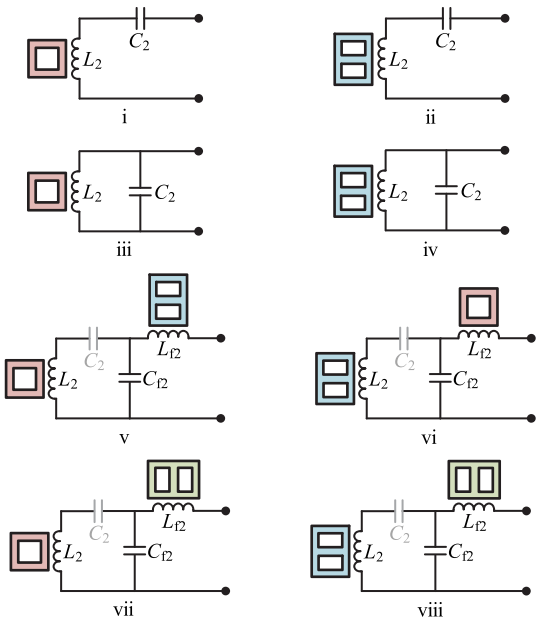


Fig. 5. Compatible Rx configurations.

TABLE I
FEASIBLE CONFIGURATION COMBINATIONS

| Primary configuration | Secondary configuration | Compensation topology |
|---|---|---|
| I | i | S-S |
| | iii | S-P |
| | v | S-*LCC* (S-*LCL*) |
| | vii | S-*LCC* (S-*LCL*) |
| II | ii | S-S |
| | iv | S-P |
| | vi | S-*LCC* (S-*LCL*) |
| | viii | S-*LCC* (S-*LCL*) |
| III | ii | *LCC*-S |
| | iv | *LCC*-P |
| | vi | Dual-coupled *LCC*-*LCC* (Dual-coupled *LCC*-*LCL*) |
| | viii | *LCC*-*LCC* (*LCC*-*LCL*) |

with the bipolar coil, and *LCC*-compensation with the bipolar and unipolar coils. Hence, the utilization of the proposed reconfigurable topology for Tx enables accommodation of diverse Rx configurations, irrespective of the type of transmission coils (unipolar or bipolar) and the type of compensation networks employed (including but not limited to S, P, *LCL*, and *LCC*). There are at least twelve kinds of configurations in total, as shown in Fig. 5. The combination of these configurations encompasses the majority of mainstream compensation topologies, as listed in Table I.

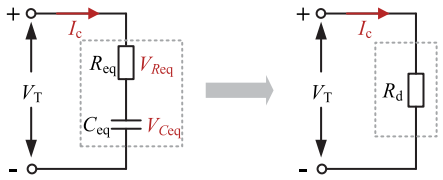


Fig. 6. *R-C* equivalent circuit of Li-ion batteries.

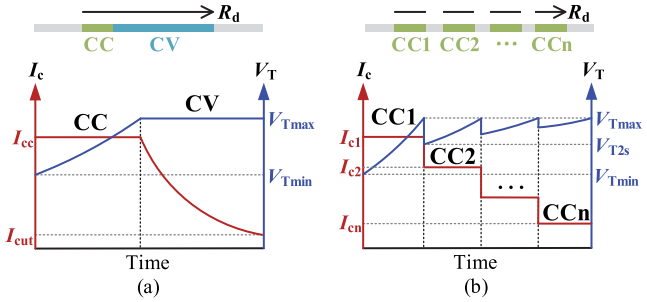


Fig. 7. (a) CC–CV charging profile. (b) MSCC charging profile.

It is admitted that the actual interoperability also depends on specific topological parameters as well as the efforts of power electronics. Nevertheless, the proposed reconfiguration and matching method alleviates the electrical burden on the inverter and improves the magnetic and electrical interoperability of IPT equipment.

## III. Analysis of the Charging Process

In this section, the equivalent dc load of a battery with two typical charging profiles is analyzed. To cope with the varying load over a wide range, the existing methods and the proposed solution are discussed.

As shown in Fig. 6, an *R-C* equivalent circuit model is used for modeling the Li-ion battery [30]. $R_{eq}$ and $C_{eq}$ denote the equivalent resistance and capacitance of the battery, respectively. During the medium to high state of charge regimes, the battery equivalent resistance $R_{eq}$ is stable [39].

When the charging current $I_c$ flows into the battery, its terminal voltage $V_T$ follows as

$$V_T = V_{Ceq} + V_{Req} \tag{6}$$

$$V_{Ceq} = \frac{1}{C_{eq}} \int_{t_0}^{t} I_c(t)\, dt + V_s, V_{Req} = I_c \cdot R_{eq} \tag{7}$$

where $V_s$ denotes the initial voltage across the equivalent capacitance $C_{eq}$. The value of $V_{Ceq}$ increases with the increase in charging time. For a power battery system with a rated voltage of $V_{T0}$, its upper limit of charging voltage is denoted as $V_{Tmax}$, and the lower limit of operating voltage is denoted as $V_{Tmin}$. Therefore, it can be approximated that $V_{Ceq}$ ranges from $V_{Tmin}$ to $V_{Tmax}$. Then, the equivalent dc load of the battery is expressed as follows:

$$R_d = V_T/I_c = V_{Ceq}/I_c + R_{Req}. \tag{8}$$

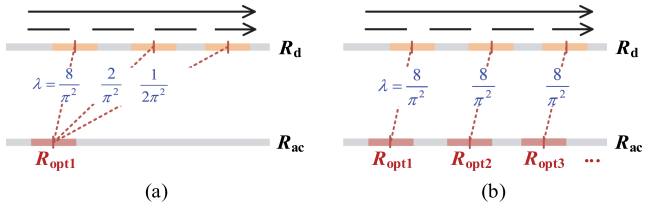


Fig. 8. Schematic diagram of methods to achieve high efficiency over a wide load range, with the colored areas representing high-efficiency regions and $\lambda = R_{ac}/R_d$. (a) Utilizing power converters and (b) utilizing reconfigurable resonant networks.

$R_d$ is greatly affected by the charging current $I_c$. Fig. 7 shows CC–CV and MSCC charging profiles. If the charging profile follows the CC–CV method, $R_d$ varies within a relatively narrow range in the CC stage; while in the CV stage, $R_d$ undergoes significant continuous variation, because the variation of current is obvious. If the charging profile follows the MSCC method, the CV stage is replaced by several CC stages with a monotonically decreasing current value. According to (8), the current $I_c$ with each value corresponds to a range of $R_d$, and multiple current values result in multiple ranges of $R_d$.

Therefore, a wide range of variation in $R_d$ is inevitable whether by CC–CV or MSCC charging method. Their differences lie in the continuity of $R_d$ and the width of actual working ranges. For IPT systems with only one optimal load value, it is difficult to maintain high efficiency throughout the whole charging process. As shown in Fig. 8(a), $R_{ac}$ represents the equivalent ac load of $R_d$. $R_{opt1}$ is the optimal ac load of a certain resonant network. As $R_d$ varies, the high efficiency is only achieved within a narrow range around $R_{opt1}/\lambda$.

To address this issue, the conventional idea is to change the ratio $\lambda$ by secondary power converters to broaden the high-efficiency region. On the contrary, it has been noticed that the optimal load value is determined by the structure and parameters of resonant networks. Therefore, another idea is conceived that if the reconfigurable topology is used, more optimal load values of $R_{opt}$ are created due to the variable structure and parameters of resonant networks, so that high efficiency can be maintained as the equivalent load of the battery varies, as shown in Fig. 8(b). And it is especially suitable for MSCC charging mode with multiple discrete intervals.

## IV. Proposed Reconfigurable Topology-Based IPT System

In this section, a novel reconfigurable topology-based IPT system is proposed first. Then, the operation modes and parameter relationships of the system are analyzed, and the load-independent output characteristic of each mode is observed. Finally, the expression of efficiency for resonant networks is derived.

### A. Reconfigurable Topology-Based IPT System

To achieve high efficiency over a wide load range while following the charging profiles, a novel IPT system based on

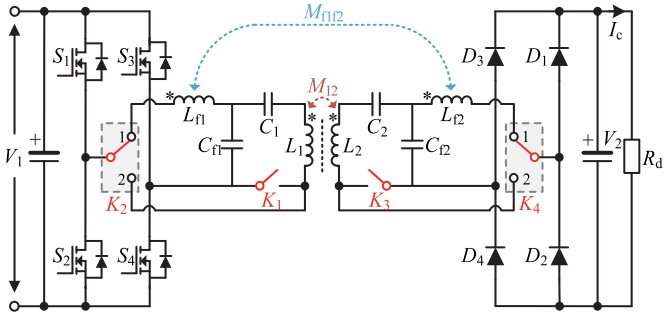


Fig. 9. Circuit diagram of the IPT system with the proposed reconfigurable topology on both sides.

the reconfigurable topology for both Tx and Rx is proposed, as shown in Fig. 9. $V_1$ is the dc-link voltage obtained from the grid-connected ac/dc converter. $R_d$ represents the equivalent dc load of batteries. $V_2$ represents the dc voltage across $R_d$. $I_c$ is the charging current. $S_1$~$S_4$ are power MOSFETs of primary-side full bridge converter. $D_1$–$D_4$ are rectifier diodes on the secondary side. $L_1$ and $L_2$ are the main coils, while $L_{f1}$ and $L_{f2}$ are the compensation inductors. The main coil $L$ and compensation inductor $L_f$ are integrated as the transmitter or receiver. $M_{12}$ and $M_{f1f2}$ are the mutual inductance of the main coils or the compensation inductors, respectively. Other compensation components include capacitors $C_{f1}$ ($C_{f2}$) and $C_1$ ($C_2$). $K_1$–$K_4$ are selector switches, where $K_2$ and $K_4$ are SPDT switches.

In fact, in addition to the $M_{12}$ and $M_{f1f2}$, there is also cross-couplings in the system. For example, $M_{1\text{-}f1}$ ($M_{2\text{-}f2}$) represents the same-side mutual inductance between $L_1$ and $L_{f1}$ ($L_2$ and $L_{f2}$), while $M_{1\text{-}f2}$ ($M_{f1\text{-}2}$) represents the different-side mutual inductance between $L_1$ and $L_{f2}$ ($L_{f1}$ and $L_2$).

Considering the magnetic flux distribution of unipolar and bipolar coils, when the central positions of these coils are aligned, the coupled magnetic flux is nearly zero. In addition, the same-side coils are consistently decoupled whether the coil centers of the receiver and transmitter are aligned or misaligned. Therefore, the same-side cross-couplings $M_{1\text{-}f1}$ and $M_{2\text{-}f2}$ are neglected in the following analysis.

As for the different-side cross-couplings, it depends on the coil integrated scheme and the misalignment direction. For scheme (c), $M_{1\text{-}f2}$ and $M_{f1\text{-}2}$ are nearly zero whether for X-misalignment or Y-misalignment due to the symmetry of the coil structure and arrangement. Similarly, for schemes (a) and (b), $M_{1\text{-}f2}$ and $M_{f1\text{-}2}$ are also nearly zero for Y-misalignment. Nevertheless, under the X-misalignment, $M_{1\text{-}f2}$ and $M_{f1\text{-}2}$ should be considered and their effect will be discussed in Section V-D.

### *B. Operating Modes Analysis and Compensation Network Modeling*

The proposed IPT system can operate in up to five modes. Fig. 10 shows the ON–OFF state of the switches in each mode. It is noted that there is no interference between these modes because only specific coils and capacitors are enabled through the selection of switches.

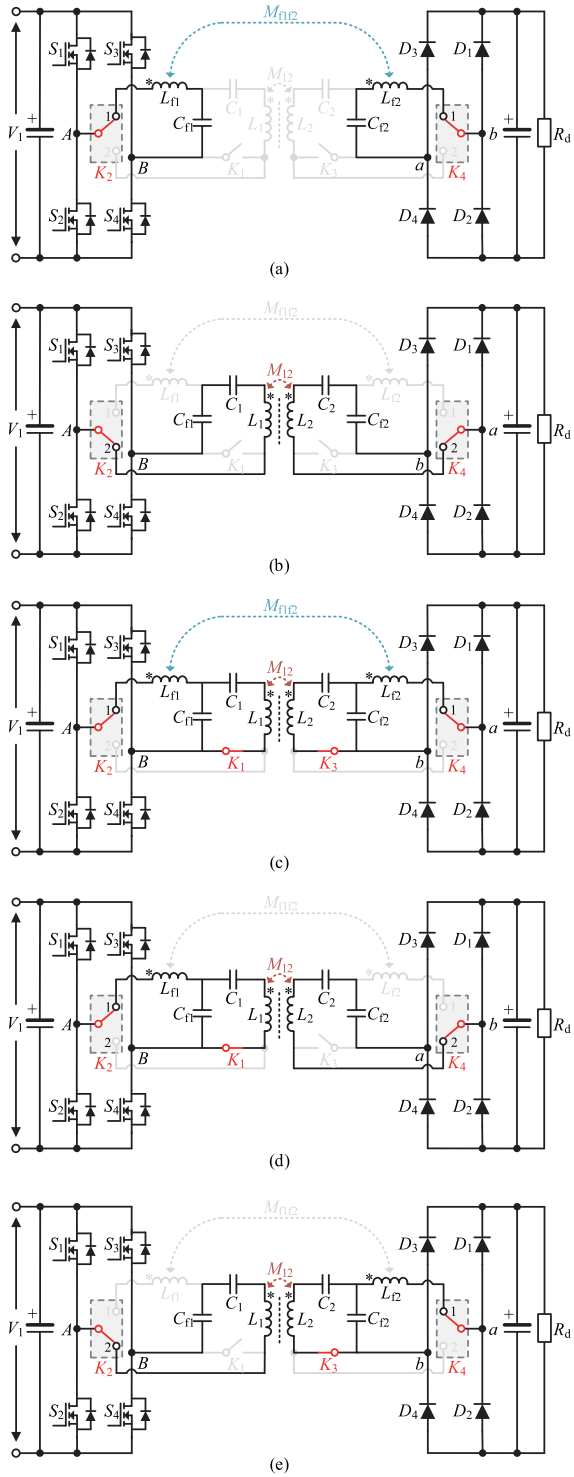


Fig. 10. Five operating modes of the proposed IPT system. (a) SS. (b) SS. (c) Dual coupled *LCC*–*LCC*. (d) *LCC*-S. (e) S-*LCC* topology.

1) *Mode a:* When $K_{21}$ and $K_{41}$ are closed, the compensation network operates as a conventional SS topology.
2) *Mode b:* When $K_{22}$ and $K_{42}$ are closed, the compensation network operates as another SS topology.

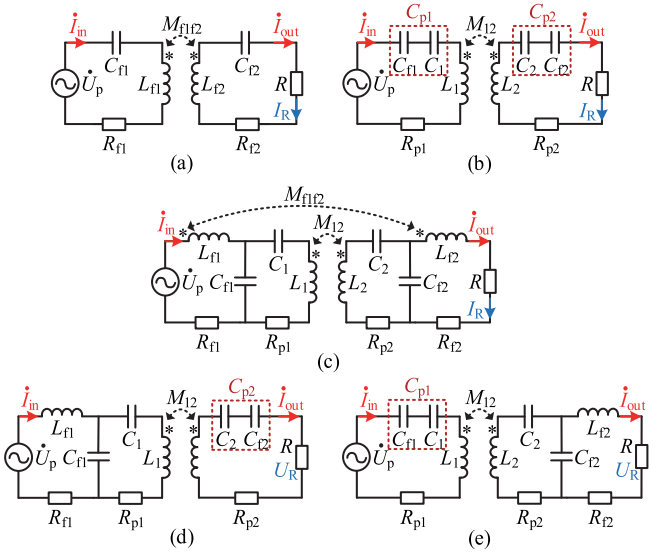


Fig. 11. Equivalent circuit of the resonant network for each mode.

3) *Mode c:* When $K_1$, $K_{21}$, $K_3$, and $K_{41}$ are closed, the compensation network operates as a dual-coupled *LCC–LCC* topology.
4) *Mode d:* When $K_1$, $K_{21}$, and $K_{42}$ are closed. the compensation network operates as a *LCC*-S topology.
5) *Mode e:* When $K_{22}$, $K_3$, and $K_{41}$ are closed, the compensation network operates as a S-*LCC* topology.

For the convenience of analysis, the fundamental harmonic approximation method is used. Fig. 11 shows the equivalent circuit of the compensation network for each operating mode. $\dot{U}_p$ represent the fundamental excitation voltages. $R$ represents the equivalent ac load resistance, and the relationship between $R$ and $R_\mathrm{d}$ follows as

$$R = 8/\pi^2 \cdot R_\mathrm{d}. \tag{9}$$

The equivalent series resistance (ESR) of inductors ($L_{\mathrm{f1}}$, $L_{\mathrm{f2}}$, $L_1$, and $L_2$), capacitors ($C_1$, $C_2$, $C_{\mathrm{f1}}$, and $C_{\mathrm{f2}}$), and switches ($K_1$–$K_4$) are denoted as $R_{\mathrm{Lf1}}$, $R_{\mathrm{Lf2}}$, $R_{\mathrm{L1}}$, $R_{\mathrm{L2}}$, $R_{\mathrm{C1}}$, $R_{\mathrm{C2}}$, $R_{\mathrm{Cf1}}$, $R_{\mathrm{Cf2}}$, and $R_{\mathrm{K}}$, respectively. Then, the ESR of each branch in different modes can be obtained by adding the ESR of the corresponding inductors, capacitors, and switches. As an illustration, $R_{\mathrm{f1}} = R_{\mathrm{Lf1}}+R_{\mathrm{Cf1}}+R_{\mathrm{K}}$, $R_{\mathrm{p1}} = R_{\mathrm{L1}}+R_{\mathrm{C1}}+R_{\mathrm{Cf1}}+R_{\mathrm{K}}$.

### C. Parameter Design

The topology parameters on the secondary side also follow a relationship similar to (1) and (2), and they are not repeated here. As shown in Fig. 11, the equivalent capacitance is

$$C_{\mathrm{p1}} = \frac{C_{\mathrm{f1}}C_1}{C_{\mathrm{f1}}+C_1}, C_{\mathrm{p2}} = \frac{C_{\mathrm{f2}}C_2}{C_{\mathrm{f2}}+C_2} \tag{10}$$

$$L_1C_{\mathrm{p1}} = 1/\omega^2, L_2C_{\mathrm{p2}} = 1/\omega^2. \tag{11}$$

Neglecting the ESRs in resonant networks, the ideal output current/voltage of the equivalent load for each mode follows as

$$\begin{cases} I_{\mathrm{R\_}a} = U_\mathrm{p}/(\omega M_{\mathrm{f1f2}}) \\ I_{\mathrm{R\_}b} = U_\mathrm{p}/(\omega M_{12}) \\ I_{\mathrm{R\_}c} = U_p M_{12}/[\omega\,(L_{\mathrm{f1}}L_{\mathrm{f2}} + M_{12}M_{\mathrm{f1f2}})] \\ U_{\mathrm{R\_}d} = U_\mathrm{p} M_{12}/L_{\mathrm{f1}} \\ U_{\mathrm{R\_}e} = U_\mathrm{p} L_{\mathrm{f2}}/M_{12}. \end{cases} \tag{12}$$

Load-independent output current can be obtained with modes *a*, *b*, and *c*; while load-independent output voltage can be obtained with modes *d* and *e*.

The relationship between the output current of resonant networks and the charging current follows as

$$I_\mathrm{c} = 2\sqrt{2}\Big/\,\pi \cdot I_{\mathrm{out}}. \tag{13}$$

The relationship between voltage on the equivalent load and battery voltage follows as

$$V_2 = \pi\Big/\,2\sqrt{2} \cdot U_\mathrm{R}. \tag{14}$$

### D. Efficiency Analysis of Resonant Networks

Taking mode *a* as an example, the power loss of the resonant network follows

$$P_{\mathrm{network\_}a} = I_{\mathrm{in}}^2 \cdot R_{\mathrm{f1}} + I_{\mathrm{out}}^2 \cdot R_{\mathrm{f2}} \tag{15}$$

where $I_{\mathrm{in}}$ and $I_{\mathrm{out}}$ is the RMS value of $\dot{I}_{\mathrm{in}}$ and $\dot{I}_{\mathrm{out}}$, respectively.

Then the efficiency of resonant networks follows as

$$\eta = (P - P_{\mathrm{network}})/P \tag{16}$$

where $P$ is the ideal transmission power without taking ESRs into account.

After calculation, the efficiency of resonant networks for each mode follows the same form of expression, and it is denoted as follows:

$$\eta = 1 - \left(\frac{1}{R}\cdot X + R \cdot Y\right) \tag{17}$$

where $X$ and $Y$ are constants related to the circuit parameters. There exists an optimal load resistance $R_\mathrm{o}$, resulting in the maximum efficiency $\eta_\mathrm{m}$ of the general resonant network. Specifically, when $R_\mathrm{o}$ = sqrt($X$/$Y$), the maximum efficiency $\eta_\mathrm{m}$ = 1–2·sqrt($X$·$Y$) can be achieved.

For a more intuitive analysis, assume the circuit parameters on the primary and secondary sides are symmetrical

$$\begin{aligned} &L_{\mathrm{f1}} = L_{\mathrm{f2}} = L_\mathrm{f}, L_1 = L_2 = L \\ &C_{\mathrm{f1}} = C_{\mathrm{f2}} = C_\mathrm{f}, C_1 = C_2 = C \\ &R_{\mathrm{f1}} = R_{\mathrm{f2}} = R_\mathrm{f}, R_{\mathrm{p1}} = R_{\mathrm{p2}} = R_\mathrm{p}. \end{aligned} \tag{18}$$

Then the inductance ratio and coupling coefficient are expressed as follows:

$$\alpha = L_\mathrm{f}/L, k_{12} = M_{12}/L, k_{\mathrm{f1f2}} = M_{\mathrm{f1f2}}/L_\mathrm{f}. \tag{19}$$

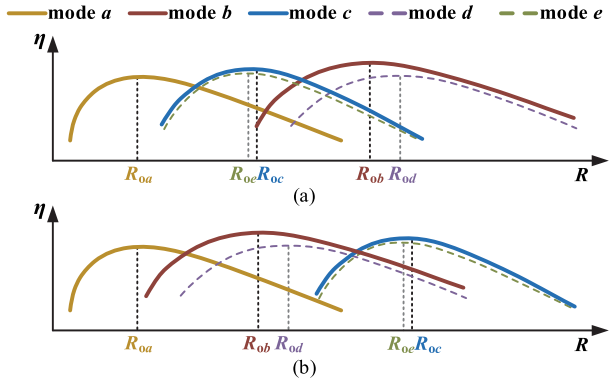


Fig. 12. Two kinds of typical efficiency-load curves for resonant networks. (a) $R_{oa} < R_{oc} < R_{ob}$. (b) $R_{oa} < R_{ob} < R_{oc}$.

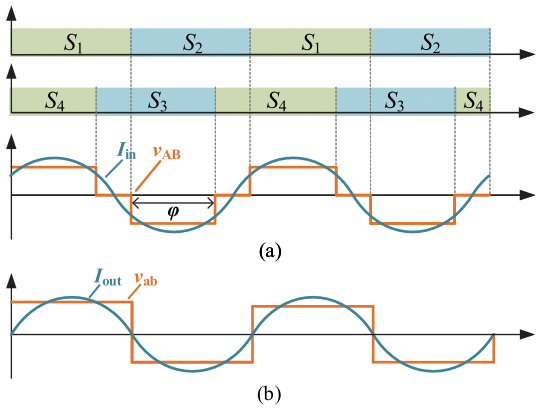


Fig. 13. Key waveforms of the (a) inverter and (b) rectifier.

Furthermore, the optimal load of each mode is written as follows:

$$R_{oa} = \omega L \cdot \alpha k_{f1f2} \tag{20}$$

$$R_{ob} = \omega L \cdot k_{12} \tag{21}$$

$$R_{oc} = \omega L \cdot \frac{\alpha^2 + \alpha k_{12} k_{f1f2}}{k_{12}} \tag{22}$$

$$R_{od} = \omega L \cdot \frac{k_{12}}{\alpha} \sqrt{\alpha^2 + k_{12}^2 \frac{R_f}{R_p}} \tag{23}$$

$$R_{oe} = \omega L \cdot \frac{\alpha}{k_{12}} \sqrt{\alpha^2 + k_{12}^2 \frac{R_f}{R_p}}. \tag{24}$$

The values of $R_f$ and $R_p$ depend on the actual coils and capacitors, as well as the adopted power switches. In this stage, their ratio is estimated approximatively using the following assumption. The quality factor is defined as follows:

$$Q = \omega L / R_p \approx \omega L_f / R_f. \tag{25}$$

Therefore, it is reasonable to obtain

$$R_f / R_p \approx L_f / L = \alpha. \tag{26}$$

It is observed that the optimal load is determined by the four key parameters ($L$, $\alpha$, $k_{12}$, and $k_{f1f2}$), thus providing sufficient design flexibility. It is obvious that $R_{oa}$ has the lowest value in any case. Besides, the value of $R_{od}$ is slightly higher than that of $R_{ob}$. And the value of $R_{oc}$ is slightly higher than that of $R_{oe}$.

From (17) and (21) to (23), when $R$ is the same, $\eta_b > \eta_d$ is always satisfied; while the relationship between $\eta_c$ and $\eta_e$ depends on the actual parameters. For simplicity, assume that $\eta_c > \eta_e$, as this inequality is more probable based on the simulations involving various combinations of key parameters.

Once the parameters are determined, the efficiency curve for each mode can be created accordingly. Two typical efficiency-load curves for resonant networks are shown in Fig. 12. In scheme (a), $R_{oc}$ is between $R_{oa}$ and $R_{ob}$. As the load resistance increases, the curves within the top region of modes $a$, $c$, and $b$ are used in turn. In scheme (b), $R_{ob}$ is between $R_{oa}$ and $R_{oc}$, and the curves within the top region of modes $a$, $b$, and $c$ are used in turn. It is observed that the relationship of $R_{ob}$ and $R_{oc}$ depends on the ratio of $\alpha$ to $k_{12}$ roughly. In other words, if $\alpha < k_{12}$, $R_{ob}$ is larger than $R_{oc}$ with a high probability; if $\alpha > k_{12}$, $R_{ob}$ is smaller than $R_{oc}$ with a high probability.

## V. Design of High-Efficiency IPT Systems With CC–CV and MSCC Charging Profiles

Although the optimal load and efficiency curve of each mode have been analyzed, only the efficiency of resonant networks is guaranteed. To achieve high efficiency at the system level, the efficiency of power electronics also needs to be evaluated. This section presents the design procedure of a reconfigurable topology-based high-efficiency system with CC–CV and MSCC outputs. Next, the method and timing of topology switching are analyzed. Additionally, the effect of misalignment on the cross-coupling of coils and the output characteristics of each mode is also examined.

### A. Control Method of the System

For tuning the mismatches between designs and practices, phase-shift control is adopted for the system, as shown in Fig. 13. For the primary side inverter, its upper and lower bridge leg switches ON and OFF complementarily with a duty cycle of 0.5 in constant resonant frequency $f$. The phase shift angle of the converter is denoted as $\varphi$.

Taking the primary fundamental voltage phase as a reference, the excitation voltage is expressed as follows:

$$\dot{U}_p = 2\sqrt{2} \Big/ \pi \cdot V_1 \cdot \sin(\varphi/2) \angle 0 = U_p \angle 0. \tag{27}$$

Each mode operates with a certain phase shift angle, and they are denoted as $\varphi_a$, $\varphi_b$, $\varphi_c$, $\varphi_d$, and $\varphi_e$, respectively.

The power losses of the inverter and rectifier are denoted as $P_{inv}$ and $P_{rec}$, respectively. And they are calculated using the formulas presented in [22]. Then, the dc–dc efficiency is expressed as follows:

$$\eta_{dc} = (P - P_{network} - P_{rec}) / (P + P_{inv}). \tag{28}$$

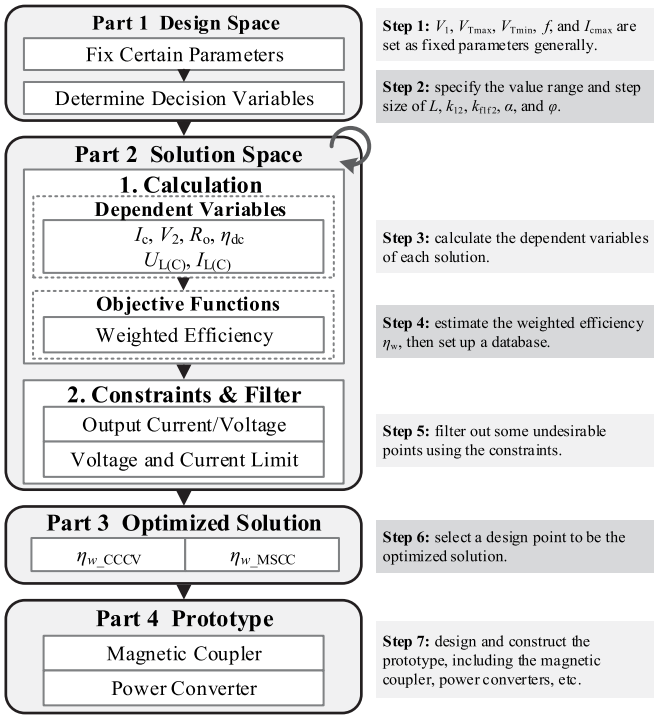


Fig. 14. Design procedure of high-efficiency IPT systems with the proposed reconfigurable topology for CC–CV and MSCC outputs.

### B. Design Procedure and Considerations

The general design procedure for a high-efficiency IPT system capable of implementing both CC–CV and MSCC outputs is shown in Fig. 14 and discussed below. To realize CC–CV output, a CC mode and a CV mode are used successively as dc load varies; to achieve MSCC output, three CC modes are adopted in turn. In fact, more CC output stages can be obtained by changing $\varphi$.

*1) Fixed Parameters and Decision Variables:* Based on actual application requirements, the dc link voltage, upper and lower limit of charging voltage, maximum charging current, and operating frequency are set as fixed parameters. The self-inductance, coupling coefficients, inductance ratio, and phase shift angle are defined as design variables. Within the feasible range of values, these parameters provide a high degree of design freedom. Next, all design solutions are obtained by traversing the design space.

*2) Objective Functions and Constraints:* For each solution, its charging current, output voltage, optimal load resistance, efficiency, and voltage/current stress are calculated first using the abovementioned equations.

After that, the objective function is defined and calculated. Each CC/CV stage corresponds to an equivalent dc load range. By calculating the efficiency corresponding to the endpoints and midpoints of each interval, and then multiplying the weight coefficients of each point, the weighted sum is denoted as the weighted efficiency $\eta_{\mathrm{w}}$ of the whole charging process.

As for the constraints, the output current/voltage should not exceed a narrow range of target output values. Besides, the solutions are constrained by voltage and current stress in coils and capacitors.

*3) Optimized Solution and Prototype Preparation:* Since there is a tradeoff between the weighted efficiency of CC–CV and MSCC charging pattern, the optimized solution can be chosen with the help of the Pareto front if necessary.

After selecting the optimal solution point, the prototype of the magnetic coupler, compensation capacitors, selector switches, and power converters is designed and constructed.

### C. Switching Method and Timing of Selector Switches

First, the issue of whether mode switching should occur online or offline is examined. If the topology switching occurs during runtime, transitioning of the transmission coils with operating capacitors can cause voltage spikes in the coils, capacitors, and selector switches, as verified by simulation. This reduces system efficiency and may damage these components. Additionally, achieving strict synchronous operation of the primary and secondary selector switches is challenging because the Tx and Rx are not physically connected. If the switching operations are not synchronized, the system may switch to unintended topologies. For instance, during a switch from mode *b* to mode *c*, if the primary side switches before the secondary side, it may first switch to mode *d* before reaching mode *c*, which is undesirable. Therefore, runtime topology switching is not recommended. For static EV charging applications, offline topology reconfiguration is more practical and feasible.

Next, the timing of mode switching is analyzed. For a Tx using the reconfigurable topology, when interfacing different Rxs, topology reconfiguration should occur before the charging process begins. Specifically, after the vehicle is parked, the onboard controller transmits information about the Rx topology via wireless communication. The Tx then switches its topology to ensure compatibility and begins power transfer. If the Rx also uses the reconfigurable topology, the reconfiguration aims to follow typical charging profiles as well as maintain high efficiency throughout the charging process, with the switching timing of selector switches depending on the charging voltage. Once the battery voltage reaches its maximum limit $V_{\mathrm{Tmax}}$, the IPT system should switch from the CC mode to the CV mode, or to the next CC mode. It should be noted that the duration for power-off, topology switching, and power-on is brief, minimally impacting the total charging time.

### D. Impact of Misalignment

The misalignments cause the variation in the self-inductance of coils. Luckily, the simulation results show that the variation is less than 2%@150 mm X/Y-misalignment, so the above analysis is not affected.

More noteworthy is the influence on mutual inductance. It is deduced from (12) that mode *a* has the highest output capacity, while mode *b* has a lower output power. At the misaligned conditions, the decrease of main mutual-inductance $M_{12}$ and $M_{\mathrm{f1f2}}$ is inevitable. This leads to the improvement of the maximum output capacity of operating modes *a* and *b*. To maintain the

TABLE II
VARIATION OF MUTUAL INDUCTANCES UNDER MISALIGNMENTS

| Misalignment direction | Mutual inductance | Coil scheme (a) | Coil scheme (b) | Coil scheme (c) |
|---|---|---|---|---|
| X-axis | $M_{12}$ | decrease | decrease | decrease |
| | $M_{f1f2}$ | decrease | decrease | decrease |
| | $M_{1\text{-}f2}$ | increase | increase | zero |
| | $M_{f1\text{-}2}$ | increase | increase | zero |
| Y-axis | $M_{12}$ | decrease | decrease | decrease |
| | $M_{f1f2}$ | decrease | decrease | decrease |
| | $M_{1\text{-}f2}$ | zero | zero | zero |
| | $M_{f1\text{-}2}$ | zero | zero | zero |

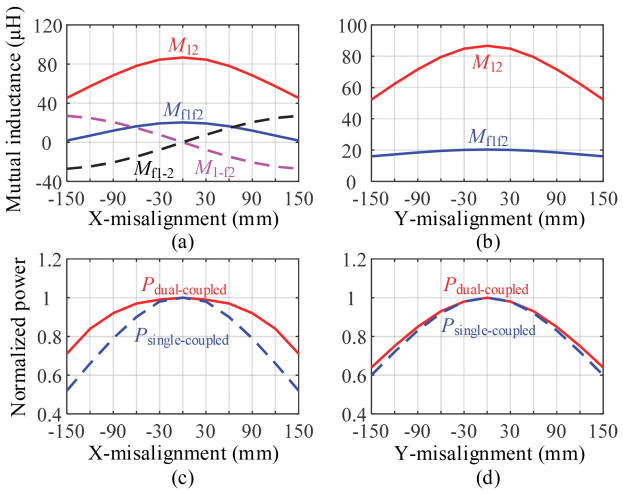


Fig. 15. Simulated mutual inductances versus the (a) X-misalignment and (b) Y-misalignment and the normalized power versus (c) X-misalignment and (d) Y-misalignment.

initial output power of mode *a*, the phase shift angle $\varphi$ of the inverter should be reduced, which increases the switching loss.

The switching between multiple operating modes provides a way to increase efficiency under misalignments. The mode that delivers the target output while minimizing light-load operation should be selected. For illustration, the main mutual inductances under aligned and misaligned conditions are denoted as $M_{12\_ali}$, $M_{f1f2\_ali}$, $M_{12\_misali}$, and $M_{f1f2\_misali}$ respectively, and can be obtained using existing mutual inductance estimation methods [40], [41]. If $M_{f1f2\_misali} < M_{12\_misali} < M_{f1f2\_ali}$ is satisfied, the system can switch to mode *b* to maintain the rated output. In this scenario, the phase shift angle of mode *b* is larger than that of mode *a*, resulting in smaller switching losses.

As deduced in the Appendix, cross-couplings under offset conditions should be considered for the other three modes, and they are summarized in Table II. For mode *c*, the number of power transmission paths is maintained at two or increased to four. Taking the integrated scheme (a) as an example, the variation of a set of mutual inductances with misalignments is obtained by simulation, as presented in Fig. 15(a) and (b). By substituting these values into (29), the normalized power with misalignments is presented in Fig. 15(c) and (d). These results prove that magnetic couplings of compensation inductors can improve the misalignment performance in comparison with

TABLE III
SPECIFICATION OF THE DESIGNED IPT SYSTEM

| Parameter | Description | Value |
|---|---|---|
| $V_1$ | Dc link voltage | 150 V |
| $V_{Tmax}$, $V_{Tmin}$ | Upper/lower limit of charging voltage | 165 V, 120V |
| $I_{cmax}$ | Maximum charging current | 9 A |
| $f$ | Operating frequency | 85 kHz |
| $H$ | Rated air gap between coils | 140 mm |

TABLE IV
OPERATION PARAMETERS OF EACH STAGE OF THE PROTOTYPE

| Charging pattern | Stage | Charging current (A) | Charging voltage (V) | Equivalent $R_d$ (Ω) |
|---|---|---|---|---|
| CC–CV | CC | $I_{cc} = 9$ | 120 –165 | 13.33 – 18.33 |
| | CV | $I_{cut} = 1$ | 165 | 18.33 – 165 |
| MSCC | CC1 | $I_{c1} = 9$ | 120 – 165 | 13.33 – 18.33 |
| | CC2 | $I_{c2} = 3$ | 150 – 165 | 50 – 55 |
| | CC3 | $I_{c3} = 1$ | 160 – 165 | 160 – 165 |

the conventional single-coupled *LCC–LCC* compensated system [42].

For mode *d* and *e*, as deduced in (30) and (31), if the cross-couplings $M_{1\text{-}f2}$ and $M_{f1\text{-}2}$ are approximately zero, the voltage gain will decrease or increase with the decrease of $M_{12}$. Otherwise, the CV output characteristics are compromised due to the introduced cross-coupling. Therefore, a constant output voltage cannot be achieved solely by the output characteristics of the topology itself; control of the input voltage $V_1$ and/or the phase shift angle $\varphi$ is also required.

## VI. EXPERIMENTAL VALIDATION

In this section, an experimental prototype is implemented to validate the proposal. The output performances are tested at the aligned and misaligned positions.

### A. Prototype Setup

In this work, the prototype is designed for charging a 150-V 18-Ah Li-ion battery with a maximum 0.5 C charging current. The specifications of the designed IPT system are listed in Table III. And the operation parameters of each stage are listed in Table IV, where $I_{cut}$ and $I_{c3}$ are predetermined values, while $I_{c2} = \text{sqrt}(I_{c1} \cdot I_{c3})$ is decided according to [30]. Combining variation ranges of the charging voltage at each stage, the equivalent dc load $R_d$ can be calculated.

The value ranges of key parameters follow as: $L \in [100, 400]$ $\mu$H, $k_{12} \in [0.18, 0.25]$, $k_{f1f2} \in [0.18, 0.25]$, $\alpha \in [0.1, 0.5]$. By traversing the design space, the feasible designs that do not violate constraints are picked out. Next, the weighted efficiency $\eta_w$ of each solution with CC–CV and MSCC charging methods is calculated. As shown in Fig. 16, the optimized solution is selected for the prototype with $L = 310$ $\mu$H, $k_{12} = 0.235$, $k_{f1f2} = 0.215$, $\alpha = 0.37$, $\varphi_{a,b,c} = \pi$, and $\varphi_e$ is around $\pi/2$. Mode *a*, *b*, *c*, and *e* are chosen as the operating mode of stages CC1(CC), CC2, CC3, and CV, respectively. Their optimal dc load is 16.2, 48.0, 135.2, and 127.6 Ω, respectively, which are located within or close to the corresponding equivalent load range.

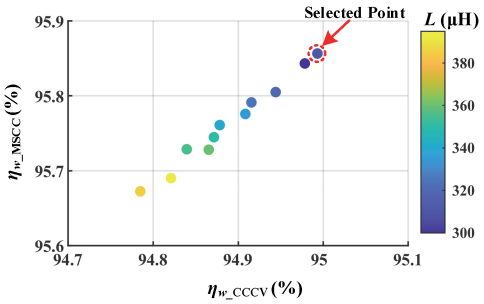


Fig. 16. Results of eligible designs, with the red line representing the selected design point.

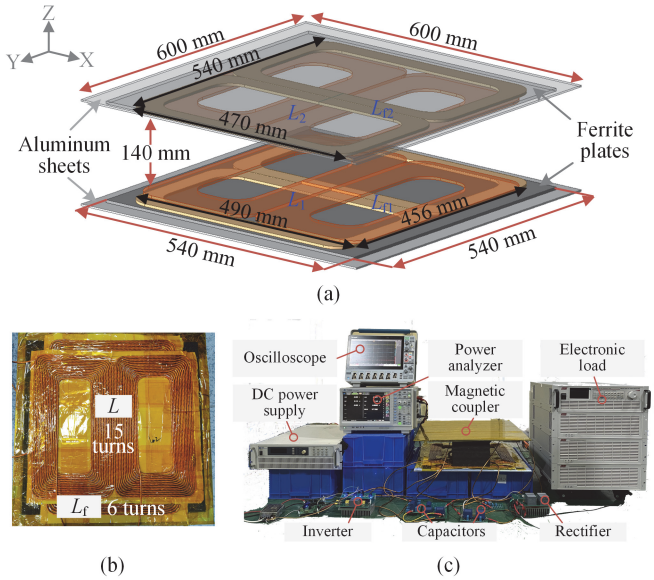


Fig. 17. (a) Diagram and (b) prototype of the magnetic coupler. (c) Experimental setup.

TABLE V
ACTUAL PARAMETERS OF THE SYSTEM PROTOTYPE

| Parameter | Measured Value | Parameter | Measured Value |
|---|---|---|---|
| $L_1$ | 311 $\mu$H | $L_2$ | 318 $\mu$H |
| $L_{f1}$ | 109.8 $\mu$H | $L_{f2}$ | 118.2 $\mu$H |
| $C_1$ | 17.37 nF | $C_2$ | 17.68 nF |
| $C_{f1}$ | 31.91 nF | $C_{f2}$ | 29.86 nF |
| $M_{12}$ | 72.5 $\mu$H | $M_{f1f2}$ | 22.75 $\mu$H |

As presented in Fig. 17(a), the designed magnetic coupler follows a typical "sandwich" construction, consisting of an aluminum shield, cores, and windings arranged sequentially. The flat aluminum backplate provides support and shielding, while a series of 5 mm thick ferrite tiles form the ferrite plate to enhance the magnetic coupling effect. And DD coils are adopted as the main coils and compensation inductors, which conforms to the integrated coil scheme (c). The constructed prototype is shown in Fig. 17(b), with the measured parameters are summarized in Table V. It should be emphasized that due to the difference between the actual and the design values, the phase shift angle also deviates from the design value to achieve target

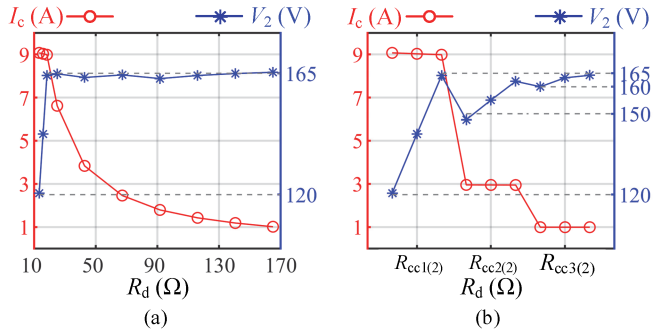


Fig. 18. Measured charging profiles of the prototype versus $R_d$. (a) CC–CV method. (b) MSCC method.

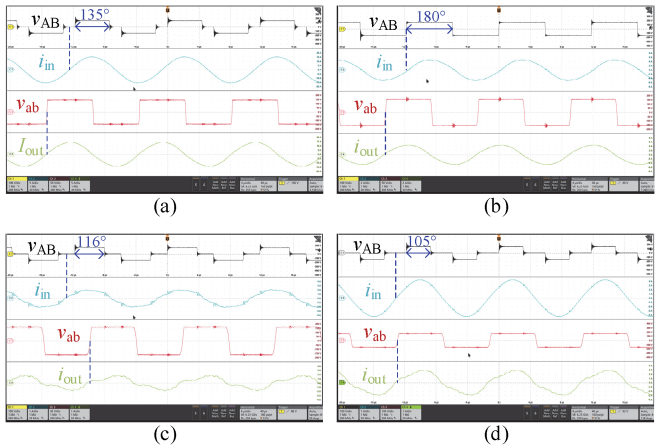


Fig. 19. Key waveforms of stage. (a) CC1 @$R_{cc1(2)}$. (b) CC2 @$R_{cc2(2)}$. (c) CC3 @$R_{cc3(2)}$. (d) CV @$R_{cv(2)}$.

outputs. In the experiment, the switching of topology is carried out manually. Besides, the MOSFETs $S_1$–$S_4$ are C3M0040120D, and the rectifier diodes $D_1$–$D_4$ are C4D40120D. The dc load $R_d$ is replaced by an electronic load (NGI N68144-1000-120). A power analyzer ZLG PA8000 is used to measure the dc–dc efficiency. All waveforms are recorded using a Tektronix MSO46 oscilloscope. The experimental setup is shown in Fig. 17(c).

## B. Experimental Results

*1) CC–CV and MSCC Output Performance:* Fig. 18 presents the measured output current and voltage for the whole charging process, where $R_{cc1(1)}$, $R_{cc1(2)}$, and $R_{cc1(3)}$ represent the start, midpoint, and end point of the corresponding dc load range for stage CC1, and the rest symbols are similar. For all CC stages, the fluctuation of the charging current $I_c$ versus $R_d$ is within 1%; for the CV stage, the fluctuation of charging voltage $V_2$ versus $R_d$ is less than 1.5%. The error between the actual output values and the target values is mainly due to the influence of high-order harmonics and ESRs of passive elements. Fig. 19 shows the key waveforms at the midpoints of different dc load ranges. The inherent load-independent CC/CV output and ZPA input characteristics for all operating modes are verified.

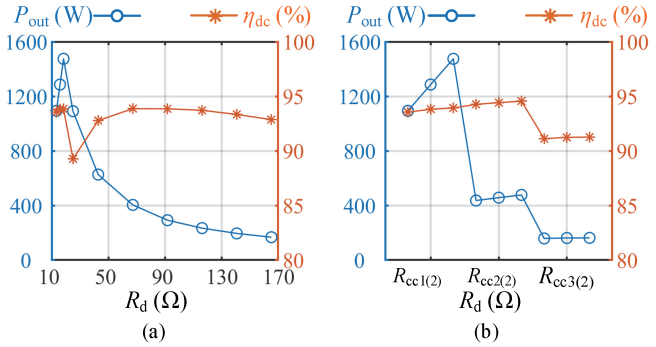


Fig. 20. Measured output power and efficiency versus $R_d$. (a) CC–CV method. (b) MSCC method.

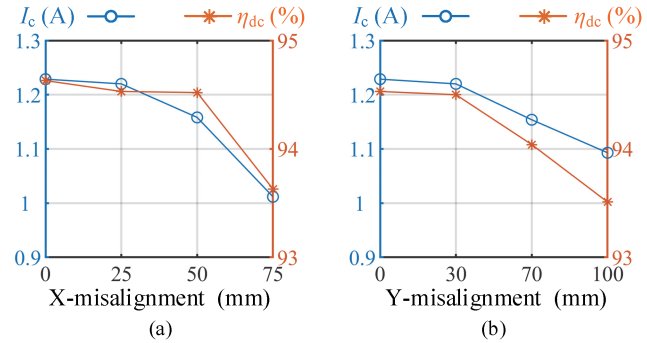


Fig. 21. Measured output of mode $c$ @ $V_1 = 150$ V, $\varphi = 180°$ versus (a) X-misalignment and (b) Y-misalignment.

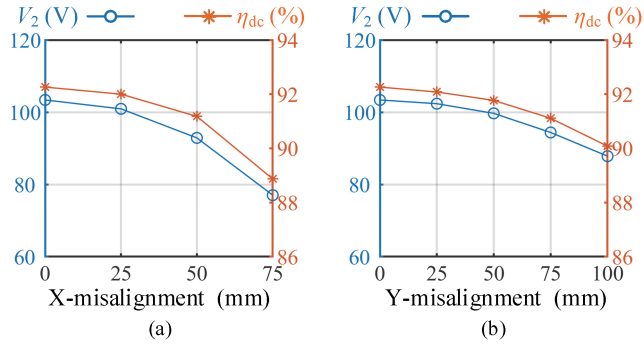


Fig. 22. Measured output of mode $d$ @$V_1 = 150$ V, $\varphi = 180°$ versus (a) X-misalignment and (b) Y-misalignment.

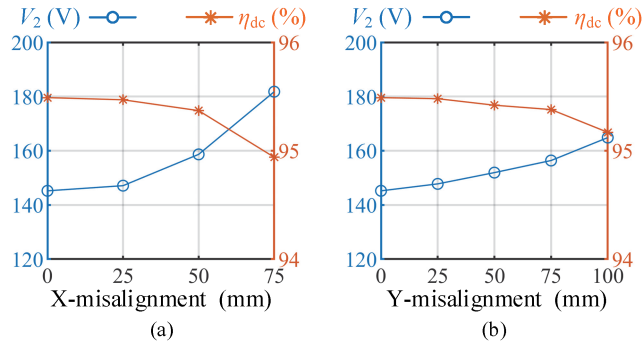


Fig. 23. Measured output of mode $e$ @ $V_1 = 100$ V, $\varphi = 180°$ versus (a) X-misalignment and (b)Y-misalignment.

*2) Efficiency Test:* Fig. 20 illustrates the measured output power and dc–dc efficiency of the whole charging process with the CC–CV method and MSCC method. The efficiency of the CC1 stage (mode *a*) is between 93.5% to 93.9%. For the CV stage (mode *e*), the transfer efficiency over the load range of 43 to 165 Ω is more than 92.7%. The operating efficiency of the CC2 stage (mode *b*) is above 94.3%. For mode *c*, there are more passive components than other modes; besides, the actual phase shift angle deviates from the designed value ($\pi$) and thus brings about switching losses. Despite this, the efficiency of the CC3 stage is still higher than 91.1%. Since the optimal loads are set within or near the operating intervals of $R_d$, the dc–dc efficiency remains consistently high throughout the charging process for both modes. Even when accounting for the conduction losses of the selector switches, these losses constitute less than 0.5% of the transmission power. This proportion could be further reduced by using bidirectional power switches with lower on-state resistance. Additionally, it is worth noting that the efficiency with the MSCC mode surpasses that with the CC–CV mode, confirming the validity of the proposed idea in this article.

*3) Misaligned Performance Test:* The output current and efficiency of mode *c* under misaligned conditions are presented in Fig. 21. The results show that the output current retains 82% at a 75 mm X-misalignment and 89% at a 100 mm Y-misalignment, with the efficiency remaining at a high level. Additionally, the output voltage of mode *d* and *e* versus misalignments are tested, as shown in Figs. 22 and 23. The experimental results indicate that the variation trend of the output voltage is consistent with the analysis.

## C. Discussion

Table VI presents a comparison between the proposed work and state-of-the-art IPT charging techniques. The proposed topology not only realizes the compatibility with basic coils but also considers the matching with various compensation networks. This approach broadens the driving region of the interface impedance and reduces the electrical burden on inverters. Moreover, the proposed IPT system based on reconfigurable topology supports two typical charging profiles and offers superior efficiency compared to other methods. The selector switches introduced are minimally complex to control and do not contribute to bulkiness. It is admitted that this technique does not offer a clear cost advantage over existing methods due to the need for four transmission coils and additional selector switches. However, while other works mainly address one or at most two issues, such as enhancing magnetic interoperability, improving electrical interoperability, following typical charging profiles, or achieving maximum efficiency point tracking, the proposed approach simultaneously addresses all these aspects. Considering the tradeoff between the gained flexibility and cost, this work remains a competitive method.

TABLE VI
COMPARISON WITH OHER RELATED WORKS

| Ref. | Charging profile | Additional components | Magnetic interoperability improvement | Electrical Interoperability improvement | Control complexity | Operating frequency (kHz) | Output power (W) | DC load range (Ω) | DC-DC efficiency (%) |
|---|---|---|---|---|---|---|---|---|---|
| [14]@2023 | / | Decoupling windings, three compensation capacitors, three DC-link capacitors, four diodes | Yes | / | Low | / | 1100 | 50 | 86 – 89 |
| [15]@2024 | / | Active rectifier, a relay, a compensation capacitor | Yes | / | Medium | 85 | ~1800 | 20 | 83 – 87 |
| [25]@2023 | / | Three relays, an L-C resonant matching network, a capacitor | / | / | Medium | 100 | ~530 | 10–600 | 89 – 92.8 |
| [31]@2023 | MSCC | / | / | / | Medium | 17, 28.33, 85 | 318 | 28.3–353.3 | 83 – 94.6 |
| [32]@2023 | MSCC | Variable inductor, semi-active rectifier | / | / | High | 85 | ~1100 | 5–51.8 | 87.4 – 92.9 |
| [33]@2024 | MSCC | Two dc capacitors, two MOSFETs, two diodes | / | / | Medium | 100 | 164 | 13–145.6 | 89.4 – 93.7 |
| [43]@2021 | CC–CV | Two switches, a capacitor | / | / | Low | 85 | 1000 | 20–100 | 87 – 91.8 |
| [44]@2023 | CC–CV | / | / | / | Medium | 85 | ~1000 | 1.2–28.7 | 79.9 – 91.6 |
| Proposed | CC–CV, MSCC | Two/four selector switches | Yes | Yes | Low | 85 | ~1500 | 18.3 –165 | 89.3 – 93.9, 91.1 – 94.6 |

## VII. CONCLUSION

A novel reconfigurable magnetic coupling resonant topology is proposed in this work. It offers compatibility with both unipolar and bipolar coils and adapts to mainstream compensation networks such as S, P, *LCL*, and *LCC* compensation. The concept of topology matching and reconfiguration enhances the magnetic and electrical interoperability of wireless chargers. Moreover, a reconfigurable topology-based IPT system is proposed for EV battery charging. It operates at a fixed frequency and does not require any additional passive components or complicated control strategies. By toggling the four selector switches, the system can switch between three CC modes and two CV modes under ZPA conditions, facilitating both CC–CV and MSCC charging profiles. Multiple optimal load values ensure that various modes consistently operate within the top regions of efficiency curves. The efficiency with MSCC profiles during the whole charging process is better than that with CC–CV profiles. In addition, the system offers practical advantages in terms of design flexibility and anti-misalignment performance. This work provides an attractive solution to address concerns related to interoperability and efficiency.

## APPENDIX

When considering the main couplings ($M_{12}$ and $M_{\mathrm{f1f2}}$) and the cross-couplings ($M_{\mathrm{f1\text{-}2}}$ and $M_{\mathrm{1\text{-}f2}}$), the equivalent circuits of resonant networks are presented in Fig. 24.

For mode $c$, by applying Kirchhoff voltage law, and substituting the relation of the compensation elements, the expression for $I_{\mathrm{f2}}$ can be obtained. Set $U_{\mathrm{R}}$ as the reference phasor, and the phase difference with $U_{\mathrm{p}}$ is defined as $\alpha$, as shown in Fig. 25.

Furthermore, the real part of $I_{\mathrm{f2}}$ is rewritten as follows:

$$\mathrm{Re}\left(\dot{I}_{\mathrm{f2}}\right) = -\frac{M_{12}b}{(b^2+ac)}\frac{U_{\mathrm{p}}\sin\alpha}{\omega}$$

$$a = 2L_{\mathrm{f1}}M_{\mathrm{f1-2}}$$

$$b = L_{\mathrm{f1}}L_{\mathrm{f2}} + M_{12}M_{\mathrm{f1f2}} - M_{\mathrm{1-f2}}M_{\mathrm{f1-2}}$$

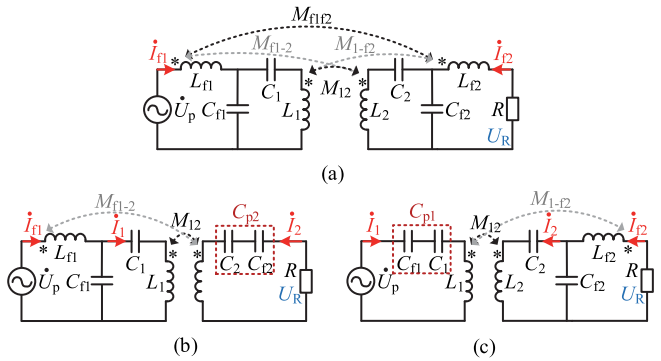


Fig. 24. Equivalent circuit of the resonant network for (a) mode *c* (b) mode *d* (c) mode *e*.

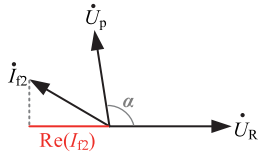


Fig. 25. Diagram of the phasors of voltage and current.

$$c = 2L_{\mathrm{f2}}M_{\mathrm{1-f2}}. \tag{29}$$

Equation (29) indicates that the four mutual inductances all affect the transmission power, and the influence of cross couplings should be considered under the offset condition.

For mode $d$, a similar analysis of the circuit shows that the expression for the output voltage follows

$$U_{\mathrm{R}} = U_p \cdot \frac{M_{12}I_1 + M_{\mathrm{f1-2}}I_{\mathrm{f1}}}{L_{\mathrm{f1}}I_1 + M_{\mathrm{f1-2}}I_2}. \tag{30}$$

Only when $M_{\mathrm{f1\text{-}2}}$ is zero, the CV output characteristic can be obtained. Otherwise, the output voltage is affected by the resistance $R$.

For mode $e$, similar patterns are observed

$$U_{\mathrm{R}} = U_p \cdot \frac{L_{\mathrm{f2}} I_2 + M_{1-\mathrm{f2}} I_1}{M_{12} I_2 + M_{1-\mathrm{f2}} I_{\mathrm{f2}}}. \tag{31}$$

Only when $M_{1\text{-f2}}$ is zero, the CV output characteristic can be obtained. Otherwise, the output voltage is affected by the resistance $R$.

## REFERENCES


[1] H. Feng, R. Tavakoli, O. Onar, and Z. Pantic, "Advances in high-power wireless charging systems: Overview and design considerations," *IEEE Trans. Transp. Electrific.*, vol. 6, no. 3, pp. 886–919, Sep. 2020.

[2] G. Ombach, D. Kurschner, and S. Mathar, "Universal base coil solution for interoperable system for stationary wireless EV charging," in *Proc. Int. Conf. Sustain. Mobility Appl., Renewable Technol.*, 2015, pp. 1–9.

[3] W. X. Zhong and S. Y. R. Hui, "Maximum energy efficiency tracking for wireless power transfer systems," *IEEE Trans. Power Electron.*, vol. 30, no. 7, pp. 4025–4034, Jul. 2015.

[4] A. Ahmad, M. S. Alam, and A. A. S. Mohamed, "Design and interoperability analysis of quadruple pad structure for electric vehicle wireless charging application," *IEEE Trans. Transp. Electrific.*, vol. 5, no. 4, pp. 934–945, Dec. 2019.

[5] W. Zhang, J. C. White, A. M. Abraham, and C. C. Mi, "Loosely coupled transformer structure and interoperability study for EV wireless charging systems," *IEEE Trans. Power Electron.*, vol. 30, no. 11, pp. 6356–6367, Nov. 2015.

[6] G. Yang et al., "Interoperability improvement for rectangular pad and DD pad of wireless electric vehicle charging system based on adaptive position adjustment," *IEEE Trans. Ind. Appl.*, vol. 57, no. 3, pp. 2613–2624, May/Jun. 2021.

[7] K. Song et al., "A review on interoperability of wireless charging systems for electric vehicles," *Energies*, vol. 16, no. 4, Feb. 2023, Art. no. 1653.

[8] M. Budhia, J. T. Boys, G. A. Covic, and C.-Y. Huang, "Development of a single-sided flux magnetic coupler for electric vehicle IPT charging systems," *IEEE Trans. Ind. Electron.*, vol. 60, no. 1, pp. 318–328, Jan. 2013.

[9] A. Zaheer, G. A. Covic, and D. Kacprzak, "A bipolar pad in a 10-kHz 300-W distributed IPT system for AGV applications," *IEEE Trans. Ind. Electron.*, vol. 61, no. 7, pp. 3288–3301, Jul. 2014.

[10] B. Jamakani, A. Mosallanejad, E. Afjei, and A. Eshkevari, "Investigation of triple quadrature pad for wireless power transfer system of electric vehicles," *Int. Eng. Technol. Elect. Syst. Trans.*, vol. 11, no. 1, pp. 58–68, Mar. 2021.

[11] A. Zaheer, H. Hao, G. A. Covic, and D. Kacprzak, "Investigation of multiple decoupled coil primary pad topologies in lumped IPT systems for interoperable electric vehicle charging," *IEEE Trans. Power Electron.*, vol. 30, no. 4, pp. 1937–1955, Apr. 2015.

[12] Y. Zhang et al., "Interoperability study of electric vehicle wireless charging system based on three decoupled non-overlapping unipolar transmitting coils," *IEEE Trans. Transp. Electrific.*, to be published, doi: 10.1109/TTE.2024.3351077.

[13] W. Pan, C. Liu, H. Tang, Y. Zhuang, and Y. Zhang, "An interoperable electric vehicle wireless charging system based on mutually spliced double-D coil," *IEEE Trans. Power Electron.*, vol. 39, no. 3, pp. 3864–3872, Mar. 2024.

[14] Y. Zhang et al., "A quadrupole receiving coil with series-connected diode rectifiers for interoperability of nonpolarized and polarized transmitting coils," *IEEE Trans. Power Electron.*, vol. 38, no. 7, pp. 8000–8004, Jul. 2023.

[15] R. Xie, R. Liu, X. Chen, X. Mao, X. Li, and Y. Zhang, "An interoperable wireless power transmitter for unipolar and bipolar receiving coils based on three-switch dual-output inverter," *IEEE Trans. Power Electron.*, vol. 39, no. 2, pp. 1985–1989, Feb. 2024.

[16] M. Hassler, F. Niedermeier, J. Krammer, and K. Diepold, "A method for interoperable interface description of inductive power transfer systems," in *Proc. IEEE PELS Workshop Emerg. Technol., Wireless Power Transfer*, 2018, pp. 1–5.

[17] D. Kraus, G. A. Covic, H.-G. Herzog, P. A. J. Lawton, and F. J. Lin, "Design and assessment of an interoperable wireless power transfer system using an impedance-based method," *IEEE Trans. Power Electron.*, vol. 38, no. 2, pp. 2768–2781, Feb. 2023.

[18] K. Tachikawa, M. Kesler, M. Danilovic, B. Esteban, O. Atasoy, and K. Yeung, "Bi-directional wireless power transfer for vehicle-to-grid: Demonstration and performance analysis," SAE Int., Warrendale, PA, USA, SAE Tech. Paper 2019-01-0870, 2019, doi: 10.4271/2019-01-0870.

[19] R. Bosshard and J. W. Kolar, "Multi-objective optimization of 50 kW/85 kHz IPT system for public transport," *IEEE J. Emerg. Sel. Topics Power Electron.*, vol. 4, no. 4, pp. 1370–1382, Dec. 2016.

[20] H.-L. Jou, J.-C. Wu, K.-D. Wu, and C.-Y. Kuo, "Bidirectional DC-DC wireless power transfer based on LCC-C resonant compensation," *IEEE Trans. Power Electron.*, vol. 36, no. 2, pp. 2310–2319, Feb. 2021.

[21] Y. Liu, U. K. Madawala, R. Mai, and Z. He, "An optimal multivariable control strategy for inductive power transfer systems to improve efficiency," *IEEE Trans. Power Electron.*, vol. 35, no. 9, pp. 8998–9010, Sep. 2020.

[22] B. X. Nguyen et al., "An efficiency optimization scheme for bidirectional inductive power transfer systems," *IEEE Trans. Power Electron.*, vol. 30, no. 11, pp. 6310–6319, Nov. 2015.

[23] S. Chen et al., "An operation mode selection method of dual-side bridge converters for efficiency optimization in inductive power transfer," *IEEE Trans. Power Electron.*, vol. 35, no. 10, pp. 9992–9997, Oct. 2020.

[24] Y. Li, Y. Yan, H. Yang, J. Hu, and Z. He, "A reconfigurable rectifier-based power improving method of free-standing two-coil magnetic field energy harvesters over a wide load range," *IEEE Trans. Power Electron.*, vol. 38, no. 5, pp. 5638–5643, May 2023.

[25] H. Yang et al., "A hybrid load matching method for WPT systems to maintain high efficiency over wide load range," *IEEE Trans. Transp. Electrific.*, vol. 9, no. 1, pp. 1993–2005, Mar. 2023.

[26] V.-B. Vu, D.-H. Tran, and W. Choi, "Implementation of the constant current and constant voltage charge of inductive power transfer systems with the double-sided LCC compensation topology for electric vehicle battery charge applications," *IEEE Trans. Power Electron.*, vol. 33, no. 9, pp. 7398–7410, Sep. 2018.

[27] J. Lu, G. Zhu, D. Lin, Y. Zhang, H. Wang, and C. C. Mi, "Realizing constant current and constant voltage outputs and input zero phase angle of wireless power transfer systems with minimum component counts," *IEEE Trans. Intell. Transp. Syst.*, vol. 22, no. 1, pp. 600–610, Jan. 2021.

[28] T. Ikeya et al., "Multi-step constant-current charging method for an electric vehicle nickel/metal hydride battery with high-energy efficiency and long cycle life," *J. Power Sources*, vol. 105, no. 1, pp. 6–12, Mar. 2002.

[29] Y.-H. Liu, C.-H. Hsieh, and Y.-F. Luo, "Search for an optimal five-step charging pattern for li-ion batteries using consecutive orthogonal arrays," *IEEE Trans. Energy Convers.*, vol. 26, no. 2, pp. 654–661, Jun. 2011.

[30] A. B. Khan and W. Choi, "Optimal charge pattern for the high-performance multistage constant current charge method for the li-ion batteries," *IEEE Trans. Energy Convers.*, vol. 33, no. 3, pp. 1132–1140, Sep. 2018.

[31] J. Liu, C. S. Wong, C. Sun, F. Xu, X. Jiang, and K. H. Loo, "Software-reconfigurable multistage constant current wireless battery charging based on multiharmonic power transmission," *IEEE Trans. Power Electron.*, vol. 38, no. 4, pp. 5586–5597, Apr. 2023.

[32] I.-W. Iam, Z. Ding, C.-F. Ieong, C.-S. Lam, R. P. Martins, and P.-I. Mak, "Optimal bivariate control strategy of multi-stage constant current charging for IPT-based wireless electric vehicle charging," *IEEE Trans. Transp. Electrific.*, vol. 10, no. 2, pp. 4513–4528, Jun. 2024.

[33] Y. Xu, Y. Li, Y. Chen, W. Zhou, R. Mai, and Z. He, "A multiple-gain-reconfigurable-rectifier-based IPT system for battery multistage constant-current high-efficiency wireless charging," *IEEE Trans. Power Electron.*, vol. 39, no. 1, pp. 1853–1869, Jan. 2024.

[34] OMEGA, "Dual solid state relays 25 and 40 Amp Vdc Input/Vac output," 2023. [Online]. Available: https://www.omega.com/en-us/control-monitoring/relays/solid-state-relays/p/SSRDUAL240

[35] A. Mojab, J. Bu, J. Knapp, A. Sattar, and D. Brdar, "Operation and characterization of low-loss bidirectional bipolar junction transistor (B-TRANTM)," in *Proc. IEEE Appl. Power Electron. Conf. Expo.*, 2022, pp. 205–209.

[36] J. Deng, B. Pang, W. Shi, and Z. Wang, "A new integration method with minimized extra coupling effects using inductor and capacitor series-parallel compensation for wireless EV charger," *Appl. Energy*, vol. 207, pp. 405–416, Dec. 2017.

[37] T. Kan, T.-D. Nguyen, J. C. White, R. K. Malhan, and C. C. Mi, "A new integration method for an electric vehicle wireless charging system using LCC compensation topology: Analysis and design," *IEEE Trans. Power Electron.*, vol. 32, no. 2, pp. 1638–1650, Feb. 2017.

[38] T. Kan, F. Lu, T.-D. Nguyen, P. P. Mercier, and C. C. Mi, "Integrated coil design for EV wireless charging systems using LCC compensation topology," *IEEE Trans. Power Electron.*, vol. 33, no. 11, pp. 9231–9241, Nov. 2018.

[39] C. Chen, Z. Wei, and A. C. Knoll, "Charging optimization for li-ion battery in electric vehicles: A review," *IEEE Trans. Transp. Electrific.*, vol. 8, no. 3, pp. 3068–3089, Sep. 2022.
[40] F. Liu, K. Chen, Z. Zhao, K. Li, and L. Yuan, "Transmitter-side control of both the CC and CV modes for the wireless EV charging system with the weak communication," *IEEE J. Emerg. Sel. Topics Power Electron.*, vol. 6, no. 2, pp. 955–965, Jun. 2018.
[41] J. Liu, G. Wang, G. Xu, J. Peng, and H. Jiang, "A parameter identification approach with primary-side measurement for DC-DC wireless-power-transfer converters with different resonant tank topologies," *IEEE Trans. Transp. Electrific.*, vol. 7, no. 3, pp. 1219–1235, Sep. 2021.
[42] F. Lu, H. Zhang, H. Hofmann, W. Su, and C. C. Mi, "A dual-coupled LCC-compensated IPT system with a compact magnetic coupler," *IEEE Trans. Power Electron.*, vol. 33, no. 7, pp. 6391–6402, Jul. 2018.
[43] D. Wang, X. Qu, Y. Yao, and P. Yang, "Hybrid inductive-power-transfer battery chargers for electric vehicle onboard charging with configurable charging profile," *IEEE Trans. Intell. Transp. Syst.*, vol. 22, no. 1, pp. 592–599, Jan. 2021.
[44] D. Wang, C. Fu, X. Bei, and Q. Zhao, "A reconfigurable half-bridge compensation topology-based WPT system with constant current and constant voltage outputs," *IEEE Trans. Circuits Syst. II*, vol. 70, no. 1, pp. 256–260, Jan. 2023.

**Baokun Zhang** (Student Member, IEEE) received the B.S. degree in vehicle engineering from the Beijing Institute of Technology, Beijing, China, in 2019. He is currently working toward the Ph.D. degree in mechanical engineering in the National Engineering Research Center of Electric Vehicles, Beijing Institute of Technology.

His research interests include the thermal design of inductive power transfer systems and bidirectional wireless power transfer.

**Junjun Deng** (Member, IEEE) received the B.S., M.S., and Ph.D. degrees in electrical engineering from Northwestern Polytechnical University, Xi'an, China, in 2008, 2011, and 2015, respectively.

From 2011 to 2014, he was a Visiting Scholar with the Department of Electrical and Computer Engineer, University of Michigan, Dearborn, MI, USA. In 2016, he joined the Faculty of Vehicle Engineering, Beijing Institute of Technology, Beijing, China, where he is currently an Associate Professor. His research interests include wireless power transfer, resonant power conversion, and high-performance battery chargers for electric vehicles.

**Zhenpo Wang** (Senior Member, IEEE) received the B.Eng. degree in automotive engineering from Tongji University, Shanghai, China, in 2000, and the Ph.D. degree in automotive engineering from the Beijing Institute of Technology, Beijing, China, in 2005.

He is currently a Full Professor with the School of Mechanical Engineering, Beijing Institute of Technology. In the past five years, he led more than ten national research projects sponsored by the National Natural Science Foundation of China, Ministry of Science and Technology of the People's Republic of China, and Beijing Municipal Science and Technology Committee. He has authored or coauthored more than 80 journal papers and 5 monopolies and has been granted 24 invention patents. His research interests include big data technology, battery safety management, wireless charging, and advanced vehicle chassis control for electric vehicles.

Dr. Wang is currently the Executive Editor-in-Chief of the Journal of Green Energy and Intelligent Transportation. He is also on the Editorial Board of the *China Journal of Highway and Transport*. He was the recipient of several national and municipal science and technology awards.